ORIGINAL RESEARCH ARTICLE

Solidification of Al12Si Melt Pool in Laser Powder Bed Fusion

Reza Ghomashchi and Shahrooz Nafisi

An understanding of the solidification characteristics of the melt pool during laser powder bed fusion, L-PBF, metal printing is essential to ensure the manufacture of sound parts. This is the main theme of this article where it is attempted to unlock the solidification black box through calculation/measurement of the main solidification parameters of cooling rate, growth rate, temperature gradient, and undercooling. The very small melt pool size and its rapid cooling hinder the application of conventional tools to extract such information. A knowledge of these parameters and their effect on the microstructure and morphology of constituent phases could help to better control the L-PBF process and indeed all the fusion-based additive manufacturing routes, to fabricate high-quality parts. Al12Si alloy solidification during the L-PBF fabrication route is examined to highlight the extreme changes in solidification parameters and their effect on the morphology and size of eutectic Si. This is because the morphology of Si controls the mechanical properties of the finished part. The Al–Si eutectic has a divorced architecture attributed to the difficulty associated with Si growth resulted from rapid solidification. The generation of a temperature gradient of about 7700 °C/mm resulted in cooling rates in the range of 1.1×10^6 °C/s and a growth rate of 140 mm/s. Such values were then used to predict the morphology of eutectic Si based on the traditional approach.

1. Introduction

Laser powder bed fusion (L-PBF), also known as Selective laser melting (SLM), is one of the additive manufacturing techniques that had drawn considerable attention as a viable net shape manufacturing process, offering a good degree of flexibility in the design of engineering parts (Ref 1). Despite tremendous benefits, there are some process-induced defects within the L-PBF printed parts, which could be alarming especially in safety-intensive applications such as the health, aerospace, or defence industry. The concerning issues include the formation of metastable phases, harmful residual stresses, anisotropic microstructures, porosity, and poor surface finishes (Ref 2-7). The formation of defects is believed to be intrinsic to the solidification of a small size melt pool over a very short time span inducing very rapid cooling rates, $\sim 10^3 - 10^6$ °C/s (Ref 4, 5, 8-12). The size of the melt pool is dependent on the L-PBF process parameters such as scanning speed and applied heat input (power) (Ref 13, 14). In addition to the small melt pool size, the very high cooling rate is also attributed to a large

Reza Ghomashchi, School of Electrical and Mechanical Engineering, The University of Adelaide, Adelaide, Australia; and **Shahrooz Nafisi**, School of Electrical and Mechanical Engineering, The University of Adelaide, Adelaide, Australia; and Rocket Lab, Long Beach, CA, USA. Contact e-mails: reza.ghomashchi@adelaide.edu.au and shahrooznafisi@gmail.com.

lateral (center to the edge of the pool) thermal gradient establishes within the very small melt pool. In addition to the lateral temperature gradient, there is a vertical depth-wise (spatial, interlayer) thermal gradient within the melt pool that is responsible for columnar grain growth. The extreme cooling rate however could be beneficial for metallic alloys through the refinement of grains and particles of the microconstituent phases, increasing solid solubility of alloy elements through super saturation of the parent phase, and introduction of segregation-free microstructures. As reported by Li et al. (Ref 15), the silicon concentration of the Al matrix of an L-PBF fabricated Al12Si alloy has increased to around 7 wt.% from the equilibrium value of 1.65 wt.%, i.e., maximum solubility at eutectic temperature. The super saturation could improve heat treatment response as a post-fabrication step to further improve mechanical properties. Furthermore, as reported by current authors and others (Ref 16, 17), the cooling rate has a tremendous effect on the equilibrium phase diagram of Al–Si alloy by moving the liquidus, solidus, and important points such as eutectic and solid solubility limit of Si in the Al matrix as shown in Fig. 1. It is concluded that by increasing the cooling rate, the eutectic point and solid solubility limit both move to the right and the eutectic temperature is depressed to lower temperatures (Ref 16, 17). That is why the issue of rapid cooling in the context of Al–Si alloys as an important engineering alloy with wide applications in the aerospace and automotive industry becomes intriguing. This is not only due to the changes in the silicon nucleation and growth parameters (Fig. 1), but also more importantly it is the nucleation and growth mechanisms and the resultant Si morphology and size that are all affected by cooling rate (Ref 18). Therefore, it becomes important both scientifically and technologically to verify these issues during L-PBF 3D printing. This is because of the important role silicon morphology and its distribution
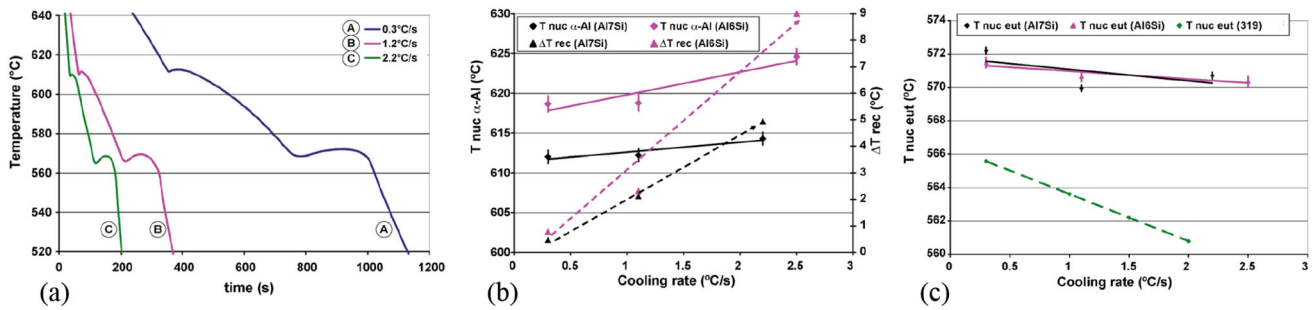
Fig. 1 (a) Effect of various cooling rates on the solidification of Al7Si and 319 alloys, (b) and (c) Variation of critical Thermal Analysis (TA) parameters with cooling rate (Ref 16). Reprinted from *Materials Science and Engineering A,* Vol 507, S. Nafisi, D. Emadi, R. Ghomashchi, Semi solid metal processing: The fraction solid dilemma, Pages 87–92, Copyright 2009, with permission from Elsevier
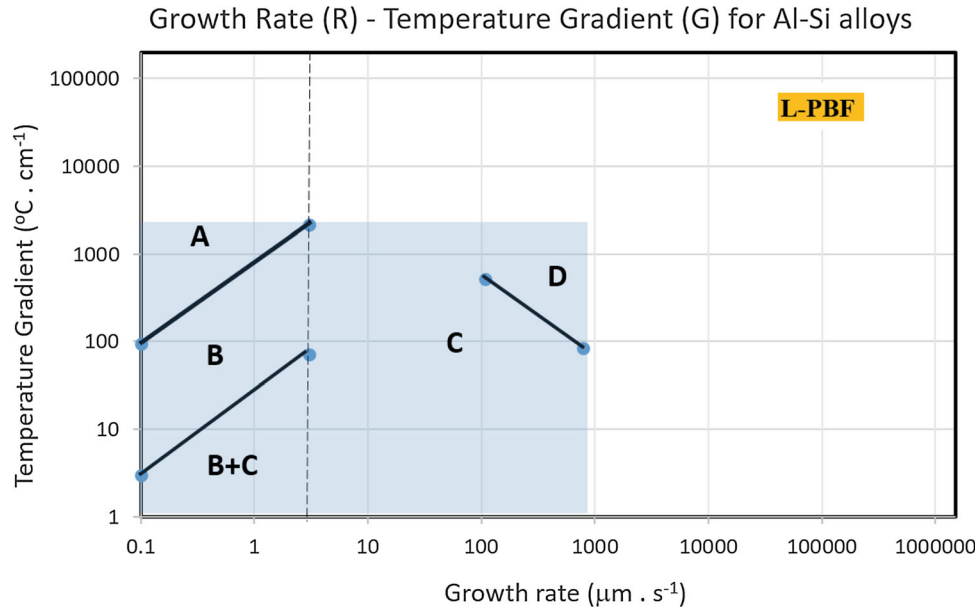

Fig. 2 Range of microstructures in directionally solidified Al–Si eutectic alloys: (A) massive particles; long-range diffusion between faceted Si particles at a planar Al interface; uncoupled growth; (B) rod or angular Si; short-range diffusion between Si rods or plates and Al; coupled growth; (C) flake Si; short-range diffusion between Si flakes and Al; partially coupled growth; (D) fibrous Si; short-range diffusion between Si fibers and Al; coupled growth, the range of growth rate with thermal gradient for L-PBF is given on the graph (the blue shaded area is reported by (Ref 18)). Used with permission of Elsevier, from *Eutectic Solidification Process,* R. Elliot, Copyright 1983; permission conveyed through Copyright Clearance Center, Inc.

play on the mechanical properties and in-service performance of the Al–Si products (Ref 19).

The silicon phase in Al–Si alloys forms with a range of morphologies controlled by solidification parameters (temperature gradient "G", undercooling "ΔT", growth rate "R", and cooling rate " $\dot{T}$" and chemical melt treatment (Sr, Na, or P modification) (Ref 18). The authors reported the true morphology of eutectic Si in a deep-etched as-cast Al7%Si alloy revealing the effect of different thermal and chemical treatments of the melt on the eutectic Si morphologies (Ref 20). The details of nucleation and growth mechanisms for silicon are well discussed in the open literature (Ref 18-25) for conventional and more advanced casting like semi-solid metal "SSM" casting (Ref 19, 26), high-pressure diecasting (Ref 27), or squeeze casting (Ref 28) where the cooling rate does not go beyond 100°Cs⁻¹. The effect of growth rate on the morphology of eutectic silicon is well represented in Fig. 2 (Ref 18). The fibrous morphology (region D on the diagram in Fig. 2), which is the result of fast cooling, forms at cooling rates around ∼ 10-

20 °C/s, which is about 3-5 orders of magnitude less than the cooling rates encountered during L-PBF 3D printing. The question is about the formation of a eutectic mixture with respect to Al and Si nucleation and their subsequent growth when the solidification rate is extremely high, almost the same as splat cooling of molten Al–Si alloys to form thin foils or strips. There is no report to specify the true 3D morphology of silicon forms during L-PBF (SLM) 3D printing despite several review articles, e.g., (Ref 29, 30), and many published research articles, e.g., (Ref 31-34): there are odd micrographs in Ref 32-34 that may give an impression of 3D-Si morphology, but not detailed enough or mentioned in the text. However, there is a recent report (Ref 15) pointing out that nano-sized spherical Si particles, surrounding a supersaturated Al matrix, form during L-PBF 3D printing without any attempt to specify if the eutectic mixture forms in the same manner reported before, e.g., (Ref 18), Al and Si duplex (co-growth), as those reported for flakes and fibrous silicon. As explained by Elliot in his excellent book on eutectic solidification (Ref 18), it is always
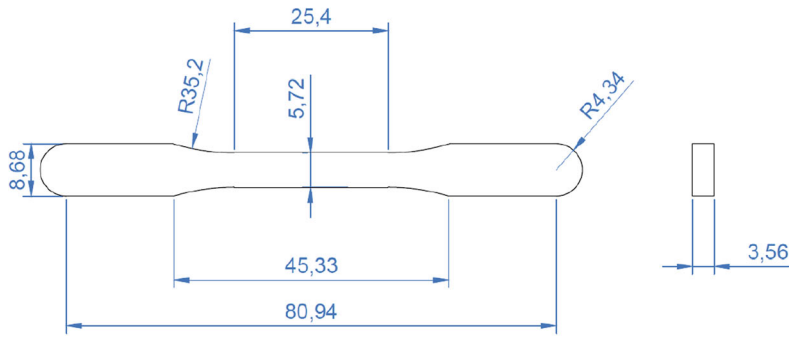
Fig. 3 Tensile samples prepared by ProX200 following ASTM E8M standard (Ref 36)

the issue of Al growth in collaboration with silicon that results in different eutectic structures, whether Al wets the silicon or not or keeps up with silicon or lags behind it. It becomes necessary to investigate the effect of cooling rate on not only the microstructure refinement but also on silicon morphology during L-PBF 3D printing. This is because of the critical role played by the morphology of silicon on the mechanical properties of Al–Si fabricated parts (Ref 35). This is the main theme of this report when L-PBF 3D printing is used to manufacture Al–Si based-alloy parts. It is attempted to estimate solidification parameters during L-PBF fabrication of Al12Si as a better correlation with the resulting microstructure. The calculated solidification parameters were also compared with simulation-estimated solidification parameters using commercially available software.

2. Material and Experimental Procedures

The Al12Si alloy powder with powder size ranging between 20 and 40 μm was used as the starting material in a ProX200 SLM 3D printing machine with the following deposition parameters;

- Laser Power: 285 W (95% of the maximum laser power of the machine, 300 W)
- Scan Speed: 2500 mm/s
- Hatch Spacing: 100 μm
- Defocus Distance: − 4 mm
- Layer Thickness: 40 μm
- Scan Pattern type: Hexagons
- Scanning Angle: ±45
- Chamber environment (gas used): Argon

The L-PBF sample geometry was based on ASTM E8M tensile testing coupons as shown in Fig. 3 with all dimensions (Ref 36). Metallographic samples were prepared from the surface, longitudinal, and transverse sections of the tensile test pieces, both from the grip and gauge length regions, polished conventionally down to 1 μm diamond paste and etched in 10% sodium hydroxide solution. For revealing the 3D characteristics of the eutectic Si phase, one of the metallographically prepared as-printed samples was deep etched for 18 min in 10% NaOH warm solution and examined under an FEI Helios Nanolab 600 SEM (FEI Dual Beam™ Focused Ion Beam Scanning Electron Microscope).
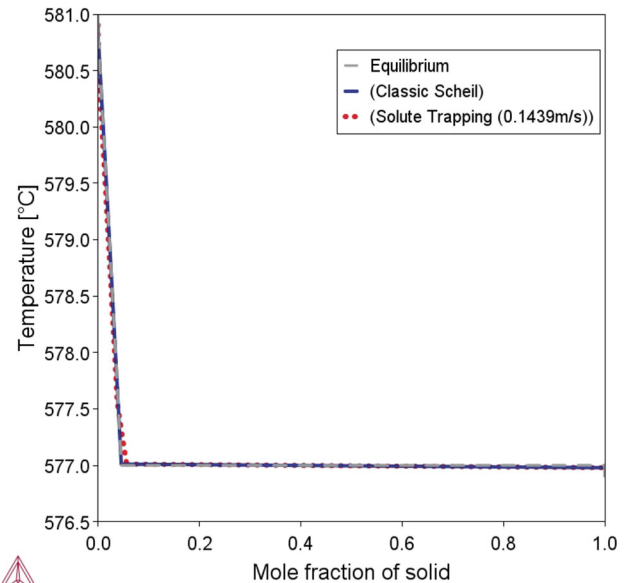

Fig. 4 Equilibrium and Scheil solidification, classical and solute trapping of the Al12Si. For solute trapping, the scan speed was 2.5 m/s with Thermo-Calc calculated solidification speed of 0.1439 m/s.

In order to have a comparison base for the eutectic silicon volume fraction, particle size, and morphology, a few of the as-printed parts were remelted in a graphite clay crucible in the lab and left to solidify in the air to produce the conventional as-cast structure as a comparison base for the as-printed constituent phases. Image J software* was used for the measurement of eutectic Si volume fraction and melt pool size.

In addition, Scheil solidification calculation was performed using Thermo-Calc 2022a** with TCAL7 database to establish the melting and the eutectic temperatures of the Al12Si alloy powder, see Fig. 4, where more than 99.95% of the constituent alloy undergo a eutectic solidification at 577 °C. The solidification simulation (fraction solid versus temperature) was performed for equilibrium, and both Scheil classical and solute entrapment, usually used for the 3D printing of powders. For

---

*ImageJ is a Java-based image processing program developed at the National Institutes of Health and the Laboratory for Optical and Computational Instrumentation (LOCI, University of Wisconsin) [https://imagej.nih.gov/ij/index.html].
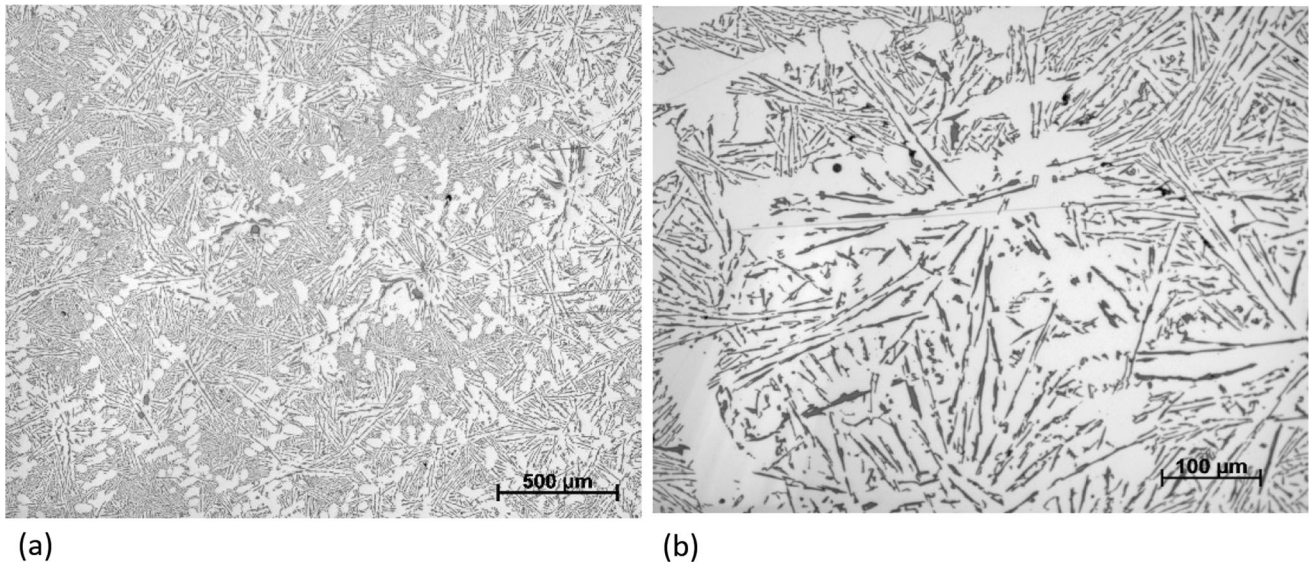**https://thermocalc.com/.

Fig. 5 Optical micrographs of the as-cast Al12Si alloy to show eutectic Al–Si along with primary α-Al dendrites (a), and eutectic Si flakes (b)

solute entrapment, it is attempted to simulate the printing condition with a scan speed of 2.5 m/s and Thermo-Calc calculated solidification speed (growth rate) of 0.1439 m/s, very close to the calculated value in this report (0.14 m/s) as given later. It is shown, Fig. 4, that there is not much difference between the graphs, but the Scheil simulation with solute entrapment has a slightly higher fraction of primary Al. This is negligible, and the inclusion of 577 °C as the melting point of this alloy (99.95%) is valid.

3. Results and Discussion

The microstructure of the conventionally cast sample, cooled in air, is given in Fig. 5 to be used as a comparison with L-PBF microstructure. The optical micrographs show the formation of primary Al dendrites in an Al–Si eutectic matrix along with the flake morphology of the eutectic Si. When the alloy is printed (L-PBF), the microstructure is refined due to the rapid solidification of a small melt pool at a time. The size of the melt pool with its cone shape geometry is measurable in Fig. 6 ranging from 50 to 80 μm (51 $\pm$ 8 μm)[†] deep and a pool cusp (diameter) of about 150-200 μm (195.5 $\pm$ 11.7 μm)^3 giving a volume (Eq 1) of $\sim$ 0.00084 mm^3 containing a weight of about 0.00223 mg (0.00223 × 10^{-3} g). The theoretical density of Al12Si is 2.6495 g/cm^3 calculated using the rule of mixture (Eq 2) (Ref 37):

$$V = \pi r^2 \left(\frac{H}{3} \right) \tag{Eq 1}$$

$$\rho_{Al12Si} = \rho_{Al} \cdot (V_f)_{Al} + \rho_{Si} \cdot (V_f)_{Si} \tag{Eq 2}$$

where V is the volume of a cone with a base radius of r and height of H. For Eq 2, ρ and V_f are the density and volume fraction of constituent phases (Al and Si), respectively. If

employing the process parameters to calculate the energy density (Eq 3), the energy input is 28.5 J/mm^3.

$$E = \frac{P}{v \cdot h \cdot t} \tag{Eq 3}$$

where E is volumetric energy density (J/mm^3), P is the laser power (W or J/s), v is scan speed (mm/s), h is hatch space (mm), and t is the layer thickness (mm).

The calculated melt pool volume was cross-checked using the FLOW-3D simulation as shown in Fig. 7. The simulation reveals that the melt pool volume could change with increasing track numbers but varies from 5 × 10^{-7} to 9 × 10^{-7} cm^3 for the first to third tracks. This is very close to the calculated melt volume of 8.4 × 10^{-7} cm^3 obtained from the optical micrographs in Fig. 6.

Knowing the weight of powder in each instant during printing, 0.00223 mg, it is possible to calculate the temperature the powder bed experiences at a time when it is irradiated by the laser beam, using the well-known thermal energy Eq 4. The first term in Eq 4 provides the energy required to bring the powder temperature to the alloy melting point. The second term is the required latent heat to enable phase change (S → L), while the third term is the energy required to bring the molten powder to a temperature above the melting point, i.e., the temperature of the molten pool:

$$Q = m \cdot c (T_m - T_0) + m \cdot \Delta H_f + m \cdot c (T - T_m) \tag{Eq 4}$$

Q is the heat input (J), m is the alloy weight (g), c is the specific heat (J/g K), ΔH_f is the latent heat of fusion for Al12Si, and T, T_m, and T_0 are the actual temperature (K); the powder bed reaches when irradiated on by the laser beam, alloy melting temperature 854 K (581 °C) as per Scheil calculation, Fig. 4, but since 99.95% of the molten alloy transforms to solid at 850 K (577 °C), all calculations are based on 850 K and the initial powder bed temperature, respectively. The powder bed and the substrate were at room temperature (T_0 = 25 °C, 298 K) at the start of printing. The latent heat of fusion was calculated using the rule of mixture for pure Al and Si (Ref 37), (560 J/g), as well as measured using Netzsch STA449, 25-700 °C at 20 °C/min, N2 purge 20 ml/min, differential scanning calorimeter, 554 J/g. The value of 560 J/g was used in this study.
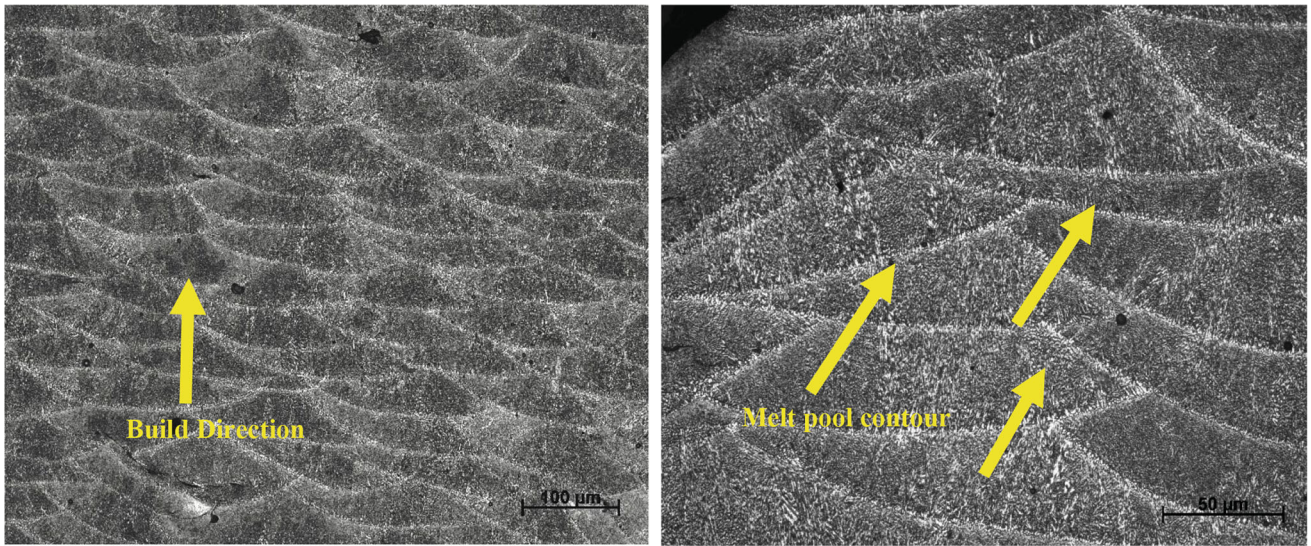

[†]Measured values on couple of optical micrographs using Image J software. The values used for weight calculation were a depth of 80 μm and radius of 100 μm.

Fig. 6 Optical micrographs of the etched longitudinal section of a tensile specimen prepared in the X direction to show the build direction and geometry of the melt pool
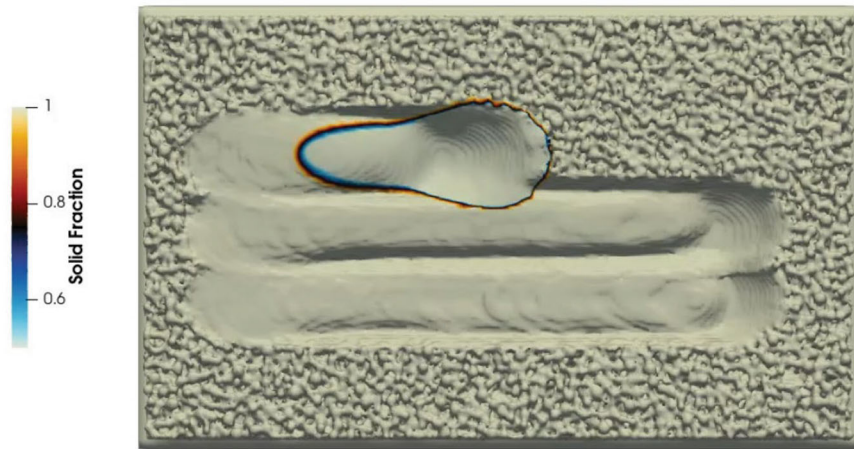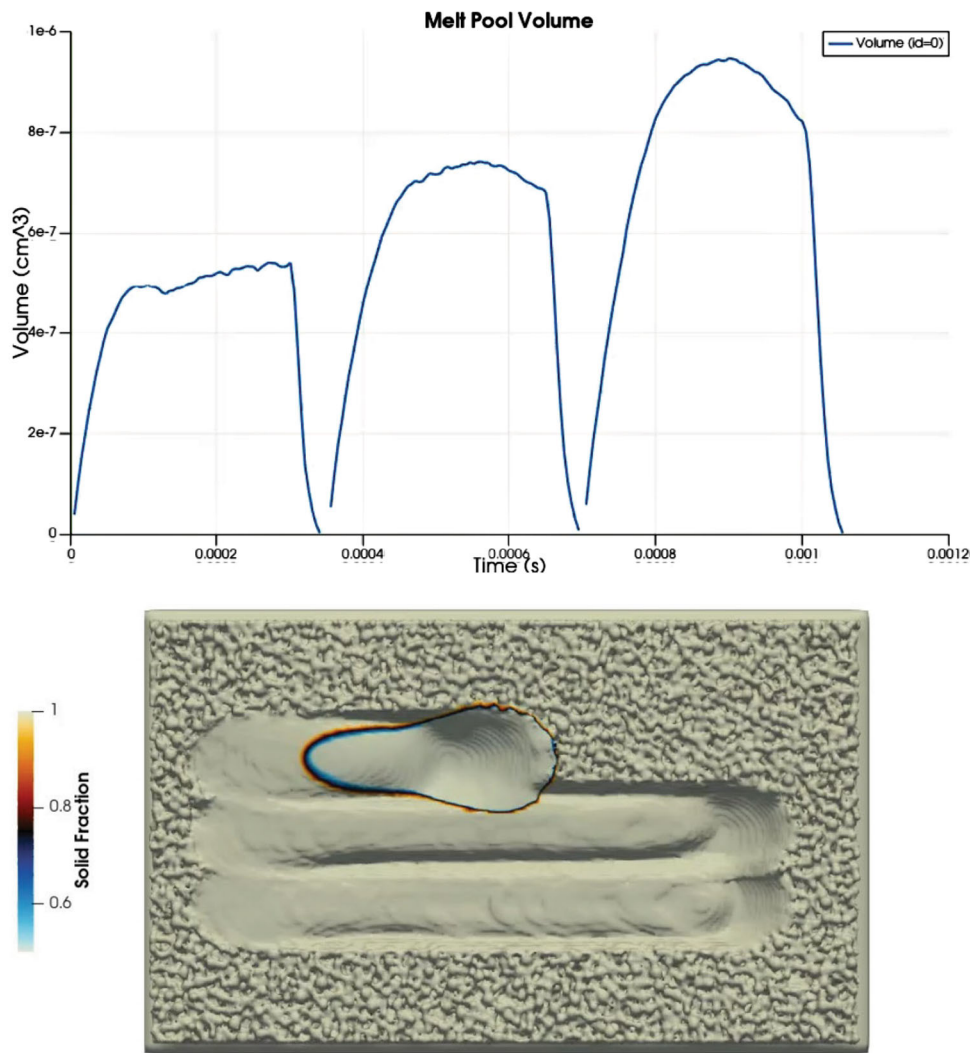

Fig. 7 Flow-3D simulation showing the melt pool volume for three tracks
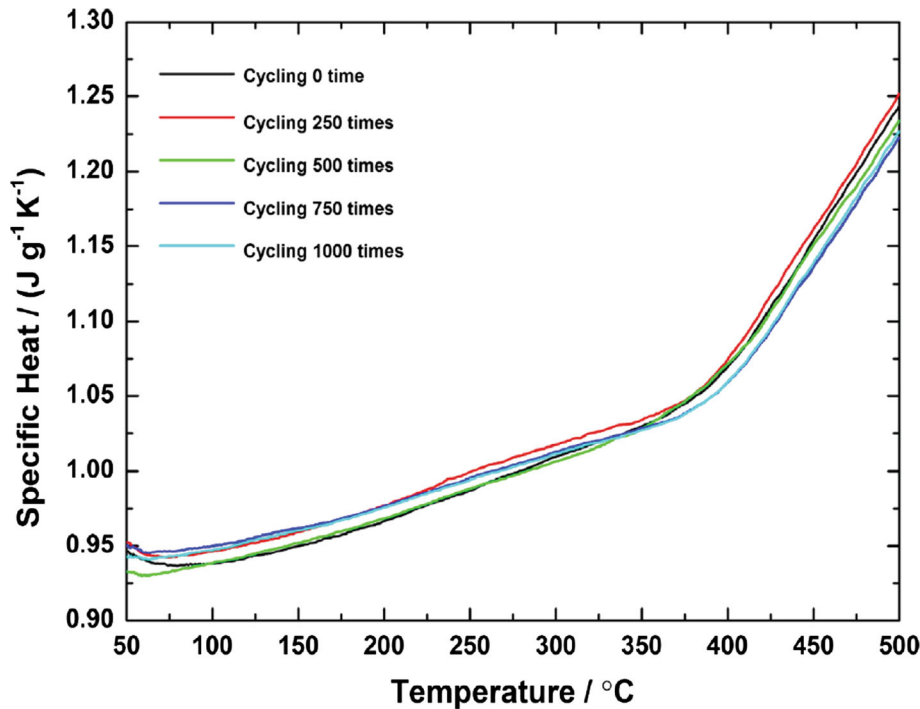
Fig. 8 The specific heat dependence of temperature of Al–Si eutectic alloy measured by DSC (Ref 38). Reprinted from *Materials Research Bulletin,* Vol 95, Zhengyun Wang, Hui Wang, Mei Yang, Wenwen Sun, Guangfu Yin, Qinyong Zhang, Zhifeng Ren, Thermal reliability of Al–Si eutectic alloy for thermal energy storage, Pages 300–306, Copyright 2017, with permission from Elsevier

The specific heat obtained from Fig. 8, (1.365 J/g K), where the linear section of the graph is extrapolated to ~ 577 °C, the melting temperature of eutectic (99.95%) alloy (Ref 38). The value obtained for specific heat from Fig. 8 is not far out from those reported for alloys with similar Si content like AlSi10Mg alloy, ~ 1.150 J/g K (Ref 39) and assumed to be almost the same for the melt pool after laser irradiation (specific heat in the third right-hand part of the Eq 4). In addition, aluminum alloys have the problem of reflecting laser beam, so the actual amount of energy absorbed by the powder bed is far less than the energy density emitted by the laser source or calculated from Eq 4. It is reported that laser reflectivity of aluminum may go as high as 91% (Ref 40) and even mentioned that the absorption for Al–Si alloys could be as low as ~ 5% only for a laser wavelength of 1060 nm (Ref 41). However, the degree of absorption or reflection is quite different for flat surfaces, polished, rough, or powders surfaces. In their calculation (Ref 42), King et al. reported an absorption factor of 1.7-7.2 times for a range of powders over flat plate metals and a value of 4.2 times for aluminum (Ref 42). When it comes to absorption of the laser beam, the value is even different for different layers, and for top layer powder, the absorption is ~ 15% for aluminum, while it is ~ 22% for the total absorptivity by the powder spheres and the substrate (Ref 42). This is coupled with high thermal conductivity (~ 239 W/m K for pure Al (Ref 43) and ~ 66-74 W/m K @ 750 °C for Al12Si (Ref 44, 45)), and thermal diffusivity (~ 70 × 10⁻⁶ m²/s, estimated from (Ref 46)) of Al alloys provides less thermal energy available for printing, resulting in the formation of pores and cracks (Ref 30). Considering only ~ 15% of the laser energy is used for melting the powder bed (Ref 42), the temperature of melt pool calculated from Eq 4 is ~ 1068 K (795 °C). If 100% of the laser energy is absorbed by the powder bed to create the melt

pool, then, the estimated temperature from Eq 4 will be ~ 7753 K (~ 7480 °C). This value is obviously not feasible as it is far beyond the boiling temperatures of both Al (2740 K/ 2467 °C) and Si (2630 K/2357 °C), and the value of ~ 1068 K (795 °C) is more acceptable. The melt pool temperature was also simulated using Flow-3D software as shown in Fig. 9 for the third track. Although the simulated temperature at the center of the melt pool where the laser beam strikes the powder bed is around 2000 K, the average melt pool temperature is around 1000-1100 K which is also in agreement with the temperature estimated using Eq 4.

In order to estimate the cooling rate, the information reported in the literature (finite element-based methods, e.g., (Ref 9, 39)) on the lifetime of the melt pool could be used to estimate cooling rate. If a lifetime of 0.2 ms is assumed (Ref 9, 39) and based on the Scheil solidification graph in Fig. 4 with 99.95% of the alloy solidifying at 577 °C, or the actual melting temperature of ~ 581 °C, a superheat of nearly ~ 218 degrees need to be extracted to have the melt pool solidify. The melt pool lifetime was also checked through the Flow-3D simulation‡, see Fig. 7, and a value of 0.15-0.18 ms was estimated for the melt pool lifetime for the first to the third track. Therefore,

---

‡The model was built using the commercially available computational fluid dynamics software, **FLOW-3D AM**. The domain encompassed a 1.1 × 0.6 × 0.1 mm solid block under a 60 μm powder bed. The material used was LM6 Aluminum with temperature dependent material properties used in calculations. Conductive wall boundary conditions were set at 293 K on the X and Y boundaries as well as the Z_{min}. An atmospheric pressure condition was set at the Z_{max} boundary at the surface of the metal, also at 293 K. The model employs Navier Stokes equations for calculating conservation of mass, momentum, and energy and the volume of fluid method for tracking the dynamics of the free surface at the gas-liquid interface. The model assumes the gas phase dynamics to be negligible and constant and uses empirical methods for calculating evaporation pressure.
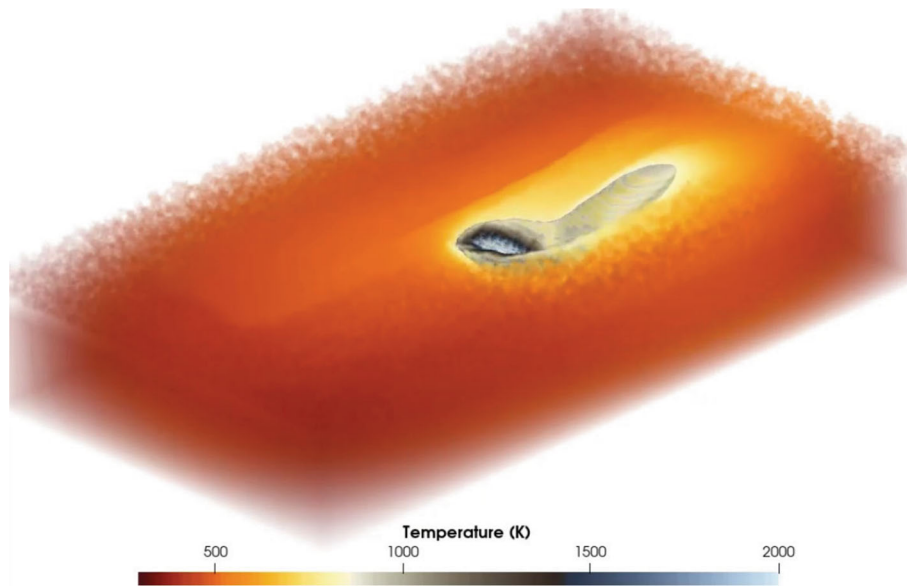
Fig. 9 Flow-3D simulation of melt pool temperature during the third track deposition for the alloy used in this study

the value of 0.2 ms from the literature appeared acceptable. This should render a cooling rate of about 1.1×10^6 °C/s. The estimated cooling rate value is close to the reported values calculated through modeling (Ref [47], [48]) considering the issue of Al alloy reflection of laser light (nearly 15% of the energy absorbed) and thermal conductivity of Al alloys compared to Ti-alloy studied in Ref [47] and the presence of TiC reinforcement in AlSi10Mg in Ref [48].

Having calculated the cooling rate, it is possible to estimate the growth rate (R) if the estimated melt pool temperature (1068 K) is used along with melt pool diameter ($\sim 200 \mu$M) to calculate the temperature gradient (G, center to edge of melt pool) during L-PBF printing of Al–Si alloys, $G = (795 - 25)/100, \sim 7.7$ °C/μm (77,000 °C/cm). The growth rate ($R = \frac{dx}{dt}$) is calculated from the relationship between cooling rate $\left(\dot{T} = \frac{dT}{dt}\right)$, growth rate (R) and temperature gradient $\left(G = \frac{dT}{dx}\right)$, i.e., $\left(\frac{dT}{dt} = \frac{dT}{dx} \times \frac{dx}{dt}\right)$; The growth rate is $R = 1.4 \times 10^5 \mu$m/s~ 14 cm/s. If the values for temperature gradient ($G \sim 8$ °C/μm) and growth rate ($R = 1.4 \times 10^5 \mu$m/s, 0.14 m/s) are superimposed on the graph in Fig. 2, it becomes obvious that the resulted morphology of Si is far beyond what specified as fibrous in region D. This means a new investigation is required to map out the important diagram established by Elliot and others (Ref [18], [21-25]) during the last quarter of the twentieth century.

The stability of interface is dependent on the G/R ratio where according to Flemings (Ref [49]), a stable interface, planar interface, is only possible at high G/R ratio (Eq 5), i.e., high G_L. Kurz and Fisher (Ref [50]) specify the critical value for G/R as (Eq 6);

$$\frac{G_L}{R} \geq -\frac{m_L(C_E - C_0)}{D_L} \tag{Eq 5}$$

$$\left(\frac{G_L}{R}\right)_{critical} = \frac{\Delta T_0}{D_L} \tag{Eq 6}$$

where C_E and C_0 are the eutectic and alloy compositions, ΔT_0 is the solidification range ($T_L - T_S$, liquidus and solidus temperatures, respectively, for the alloy composition, C_0). The diffusivity of Si (D_L) within molten Al–Si liquid was calculated by Qin et al. (Ref [51]) to be 8.8×10^{-9} m²/s (estimated from Figure 1 in Ref [51]). The solidification range for Al12Si as per Thermo-Calc calculation, Fig. 4, is 3.6 °C. This gives a critical G/R ratio of 4×10^8 °C s/m². The value of G/R calculated for the current work is 0.55×10^8 °C s/m². This is 8 times less than the critical value which means the interface will not be stable, and the formation of aluminum cells and/or dendrites should be expected during L-PBF.

In addition, according to Toloui and Hellawell (Ref [52]), the following relationships 7 and 8 hold between inter-silicon spacing (λ) and undercooling with growth velocity (R) and temperature gradient (G) in Al–Si eutectic;

$$\lambda \approx A R^{-1/2} G^{-1/3} \tag{Eq 7}$$

$$\Delta T \approx B R^{1/2} G^{-1/2} \tag{Eq 8}$$

where A and B are constants with values of 5 μm $(\mu$m/s$)^{1/2}$ (°C/μm$)^{1/3}$ and 10 °C (°C/μm$)^{1/2}$ $(\mu$m/s$)^{-1/2}$, respectively (Ref [52]). Using the above equations, it is expected to have an inter-silicon spacing of ~ 7 nm and an undercooling of about ~ 1300 °C during L-PBF process for Al12Si. It is worth noting that the Eq [7] and [8] given by Toloui and Hellawell (Ref [52]) are mainly based on a low growth rate from 20 to 400 μm/s and temperature gradients from 0.0007 to 0.0150 K/μm where the flake Si morphology is expected to form. Such values are far out from the solidification regime encountered during L-PBF, but with approximation, it may crudely be used as an indication for the Si phase that forms during L-PBF. The estimation given for inter-Si spacing will be further discussed later in this article when the morphology of eutectic Si is examined using deep etching and high-resolution SEM analysis. For undercooling however, it is difficult to accept if the calculated value of 1300 °C is valid. Since there is not any thermal analysis method to measure undercooling in the melt pool during L-PBF
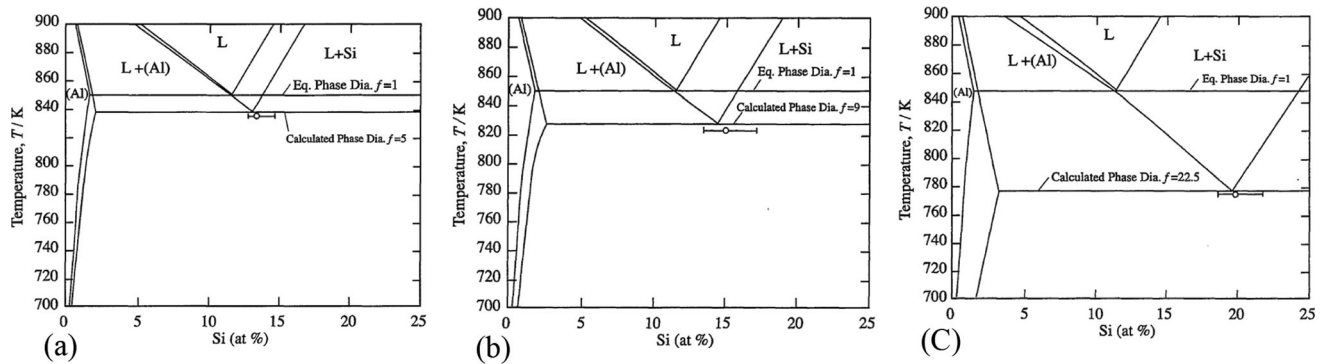
Fig. 10 Calculated phase diagram for samples solidified at cooling rates of: 16.8 °Cs⁻¹, growth undercooling 13.1 C, (b) 76.9 °Cs⁻¹, growth undercooling 25.4 C, and (C) 129.9 °Cs⁻¹, growth undercooling 29.1 C (Ref 17)

printing, a microstructural approach is implemented here to calculate the undercooling. The proposed method is based on the effect of cooling rate on the movement of eutectic point to the right (composition) and lower temperature (Ref 16, 17). This concept is used in conjunction with calculating Al and Si phases contents of the L-PBF samples and application of inverse lever rule to estimate the eutectic temperature. The difference between the melting temperature of the alloy, 580 °C, and the calculated new eutectic temperature, depression due to rapid solidification rate, should provide a more realistic value of undercooling during L-PBF printing.

The effect of cooling rate on the phase diagram however could reasonably be demonstrated as reported by the current authors (Ref 16) and (Ref 17), specifying there are changes in eutectic composition and temperature with increasing cooling rate. In a study performed by El-Benawy et al. (Ref 17), thermal analyses of various Al–Si alloys were examined in a wide range of cooling rates from 0.033 to 10^5 °Cs⁻¹ using DTA and levitation casting techniques. Figure 10 shows the calculated phase diagram at various cooling rates (Ref 17). In line with the authors studies [e.g., (Ref 16)], the higher cooling rates resulted in shifting the eutectic point to the right (i.e., higher silicon contents) as well as to the lower temperature. Accordingly, the maximum solubility of Si shifts from 1.65 to about 4 wt.% Si. Li et al. (Ref 15) also reported an increase in Si content of Al to around 7%. Our own EDS analysis of the bulk samples showed Si content of Al cell to be around 9%, although it is believed Si particles at the vicinity of the point of analysis interfered in measurement, i.e., EDS analysis of bulk samples is not the suitable method for Si content measurement of Al cells. The work of Li et al. (Ref 15) who used STEM analysis of thin foils is more reliable.

Quantitative metallography was carried out on the as-printed samples, (see SEM micrographs in Fig. 15), to measure the cell size and number of cells per unit area. A linear intercept analysis and counting the number of cells per unit area resulted in a cell size of about ~ 0.300 μm and roughly 7 Al cells per μm², respectively. Using the Eq (9) by Dehoff (Ref 53), the measured number of cells per unit area (N_A) was converted to number of cells per unit volume (N_V);

$$\overline{N_A} = N_V \overline{D_V} \qquad (Eq 9)$$

$\overline{D_V}$ is the distance between two parallel tangents on the grain/particle in a selected orientation. If it is assumed the $\overline{D_V}$ value is the same as the cell size, 0.300 μm, then, the N_V could be calculated, i.e., 23 Al cells per unit volume (μm³).

Considering that the cell size is estimated at 0.300 μm, the fraction of volume occupied by Al is, $23(0.3 \times 0.3 \times 0.3) = 0.62$ μm³/μm³ and 0.38 μm³/μm³ Si. This is equivalent to having volume fraction of Al cells in the microstructure at 62%, and the Si content is 38%. Using the reverse level rule, an Al–Si alloy with 62% aluminum is equivalent to an Al–Si alloy with Si $\cong$ 4.8%. This means rapid cooling has resulted in pushing the alloy composition to generate a microstructure that is expected from Al 4.8% Si alloy. In other words, the eutectic composition was pushed by 12.0-4.8 = 7.2% to the right due to rapid cooling during L-PBF.

If the diagram in Fig. 10(c) (Ref 17) is used with a eutectic point pushed to (12.6 + 7.2) 19.8% Si, the equivalent eutectic temperature has dropped to 778 K (505 °C). This means that the eutectic line has been pushed down to 505 °C from the equilibrium/Scheil, Fig. 4, 577. This is considered for the calculation of the undercooling of 577 − 505 = 72 °C and not 1300 °C as calculated from Toloui and Hellawell (Ref 52) equation. This confirms the importance of the solidification parameters on the solidification mechanism and the morphology of Si. If the values of 1300° and 72° are used in Eq (10) (Ref 54), the nuclei size for both undercoolings is 3.4 and 61 nm, respectively. Knowing the aluminum atomic radius of 0.143 nm, it is more realist to have a nucleus of 61 nm radius (cluster of 426 atoms) than 3.4 nm (cluster of only 24 atoms). The former is more energetically stable with much smaller surface area/volume ratio to be considered as nucleus than the latter:

$$r^* = \frac{2\gamma T_m}{\Delta H_f \Delta T} \qquad (Eq 10)$$

The value of surface tension for Al12Si is 0.8 N/m (Ref 55), T_m = 580 °C for the alloy, ΔH_f = 211 × 10^6 J/m³ (conversion of 560 J/g to J/m³ using the calculated density of 2.6495 g/cm³ for Al12Si).

The change in eutectic temperature was also calculated through measurement of the Si volume fraction from SEM micrographs using Image J. The values obtained for specimens prepared from the L-PBF printed test piece, Fig. 15, were (12.48 ± 2.3)%. If the value of 12.48% Si phase particles in the microstructure for L-PBF samples is used in a reversed lever rule calculation at room temperature assuming that the solid solubility of Al cells has increased to 7% (Ref 15) due to rapid solidification during L-PBF ($C_{Si\ in\ Al}$ = 7 wt.% (Ref 15), $C_{Si\ alloy}$ = X wt.% and $C_{Si\ eutectic}$ = 12.6 wt.%), the alloy composition comes to $\sim$ 7.7 wt.% Si. This means that the

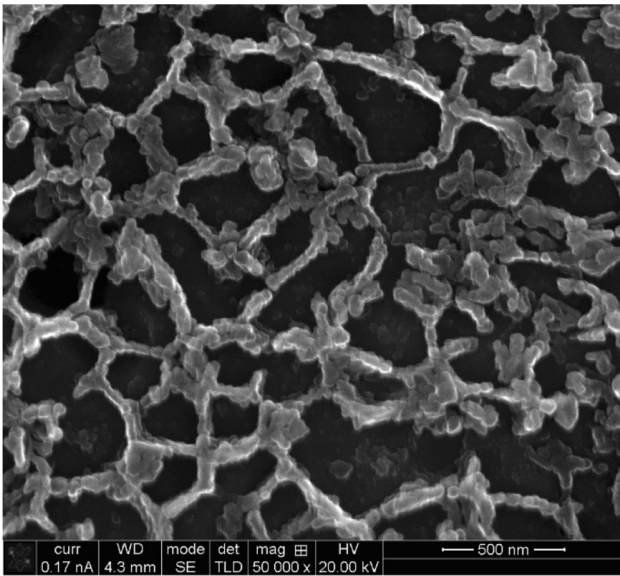**Fig. 11** SEM micrograph of the surface layer of tensile test pieces printed in Y-direction showing an Al-cell structure of around 250-400 nm

Fig. 12 SEM micrographs of the eutectic Si forming as agglomerated particles of around 5-10 nm size. The samples prepared from the surface of the tensile test pieces printed in Y-direction

alloy composition was reduced from 12 to 7.7%, a reduction by 4.3% or the eutectic point pushed to the right by 4.3%; the new eutectic composition is 16.9%. Using the Al–Si phase diagram reported by (Ref 17), Fig. 10(c), the value of eutectic temperature for ~ 17 Si% eutectic composition is about 780 K (507 °C). This provides an undercooling of 70 °C which is almost the same as that calculated above through analysis of the number Al cells per unit volume.

The as-printed Al12Si alloy was examined under a FEI Dual Beam™ Focused Ion Beam Scanning Electron Microscope (FEI Helios Nanolab 600) to resolve the silicon morphology. The SEM micrograph in Fig. 11 provides an overview of the eutectic Si resembling the fibrous morphology as reported in the open literature, e.g., (Ref 18). However, when examined more closely, it becomes apparent that the eutectic silicon morphology is more like spongy agglomerated nano-size silicon particles as shown in Fig. 12. The size of particles is around 20-50 nm, but if these particles are examined closely, it is evident that they are an agglomeration of much finer particles, as small as about 5-10 nm (Fig. 12). Furthermore, the eutectic mixture does not appear to have the same architecture of duplex (co-grown) Al and Si phases, Fig. 11 and 15 as seen in the conventional cast shown in Fig. 5.

To further reveal the true morphology and the architecture of the eutectic Si during L-PBF, the actual size of each Si particle along with its growth in build direction in Al12Si alloy, the deep-etched SEM micrographs are presented in Fig. 13 and 14. The higher magnification SEM micrograph in Fig. 14 which is taken parallel to build direction clearly shows the formation of Si particles in every layer, indicating that the formation of Si is intermittent and at short intervals joining together to form an agglomerated spongy eutectic Si. The resulted morphology is neither flake nor fibrous as specified for conventional casting route, but a new agglomerated spherical morphology. Detailed TEM analysis is required to establish the crystallographic relationship between Al and Si as well as the mechanism of Si nucleation and growth similar to that explained by Elliot in his book for conventional casting (Ref 18).
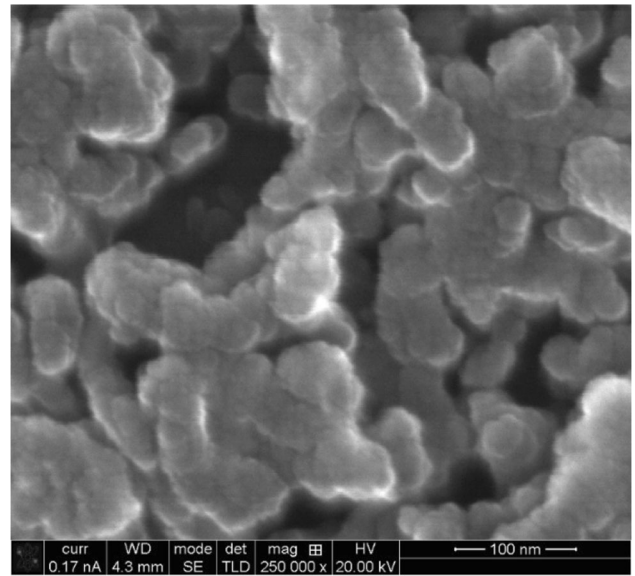
In order to explore the growth architecture of the eutectic mixture, the as-printed metallographic specimens were sputtered by Ga ions to create a wedge, (in both directions longitudinal, and transverse to eutectic Si growth direction) to allow examine the Z-direction characteristics of the eutectic mixture, Fig. 15. The SEM micrographs of the Z-cut surface in Fig. 15 reveal that the Al–Si eutectic has a divorced architecture with Si particles forming at the aluminum cell boundaries. Such divorce morphology is also detectable when the deep-etched samples, Fig. 13 and 14 or the surface layer of the tensile test samples, Fig. 11, are examined.

The formation of divorced eutectic is predictable if the nature of the interface for Al and Si is considered in conjunction with extreme cooling rate and large undercooling. Since Al has a diffused (rough) interface, such extreme conditions are less critical to its growth architecture than Si with a smooth faceted interface, where diffusion becomes difficult (Ref 56). This means the difficulty of coupled nucleation and growth of Si and Al, leaving Al to continue freezing out separately. Therefore, the Al phase is expected to form first with Si segregating at the cell boundaries. Furthermore, the deep-etched micrographs in Fig. 13 and 14 clearly demonstrated the architecture of growth for Si eutectic, i.e., divorced growth.

The agglomerated spongy nature of the Si morphology may be attributed to the solidification of a small amount of liquid at a time, small pool size, large undercooling, and high cooling rate. However, due to the diffuse nature of the Al interface, Al grows continuously as the melt pool moves during printing, irrespective of the high cooling rate of 1.1×10^6 °Cs^{-1}. The laser beam remelts the previous layer enabling epitaxial growth as new layers are printed. It is believed the remelting of Al takes place, while the Si within the prior layer does not re-melt as Al and Si are distinctly apart, and the remelting temperature does not reach the melting temperature of Si, 1414 °C. That's why the Al phase appears continuous, while Si appears as small
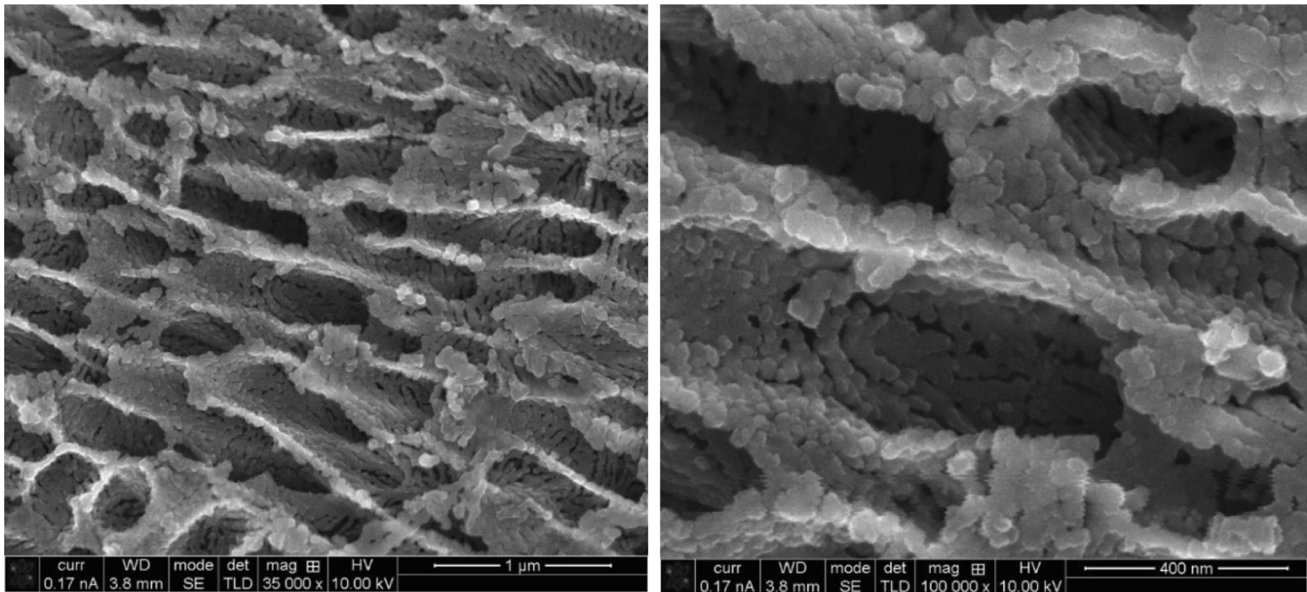
Fig. 13 SEM micrographs of deep-etched as-printed tensile samples, printed in X direction, to show the 3D growth characteristics of the eutectic Si
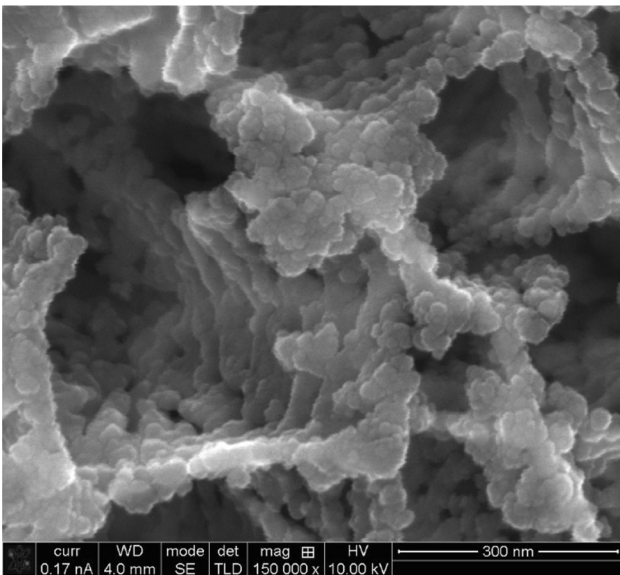

Fig. 14 Deep-etched SEM micrograph of tensile test piece samples printed in X direction to show the Si morphology along the build direction. The formation of individual particles and their agglomeration is indication of intermittent Si formation during L-PBF within each layer.

rounded particles superimposed on the previous layer giving the impression of a spongy morphology.

In addition, it is reported that the characteristic diffusion distance (l_d) decreases with growth velocity (R), $l_d = 2D/R$, (D is the solute diffusion coefficient) (Ref 57). At a critical growth velocity, the diffusion field becomes shorter in its extent than the microstructural scale (the microstructural scale here is the inter-silicon spacing calculated from Eq 7, ~ 7 nm). Diffusion, therefore, becomes localized with respect to the microstructure when $2D/R < \lambda$ (Ref 54). The value of l_d is calculated here to be 0.25×10^{-20} cm (0.25×10^{-13} nm), which is much smaller than the inter-silicon spacing. The value for D was considered as the diffusivity for self-diffusion of Si, $D = 1.8 \times 10^{-20}$ cm^2/s at 795 °C (Ref 58) and $R = 14$ cm/s as calculated in this study. This means that the Si phase nucleates on previous Si particles, and due to the very small diffusion zone, can only grow to a limited size. Therefore, in every step of melt pool formation, both the rapid growth and very short diffusion distance result in the formation of fine Si particles attached to one another. Due to such manner of growth, Si size and inter-Si spacing are almost the same and the overall Si morphology appears spherical and agglomerated.

4. Conclusions

The development of microstructure during L-PBF printing of Al12Si has been studied to highlight the concept of solidification during L-PBF deposition and at the same time expand on the formation of eutectic Si and its morphology. The approach employed for the analysis of the solidification parameters should be useful for any fusion-based 3D printing process of any metallic material. In other words, the main finding of this study is to demonstrate the application of standard equations to measure some of the important solidification and process parameters as well as how a standard simulation software could assist the users to have a better understanding of the solidification of melt pool during L-PBF process; a reliable match was found with standard commercial simulative software.

As it is well-established by the solidification research community, the magnitude of cooling rate, growth rate, temperature gradient, and undercooling are the deciding factors in the development of microstructure and morphology of constituent phases in engineering alloys. This is an important issue in Al–Si alloy performance in service as the Si morphology is the key point controlling the mechanical properties. A quantitative approach was implemented to
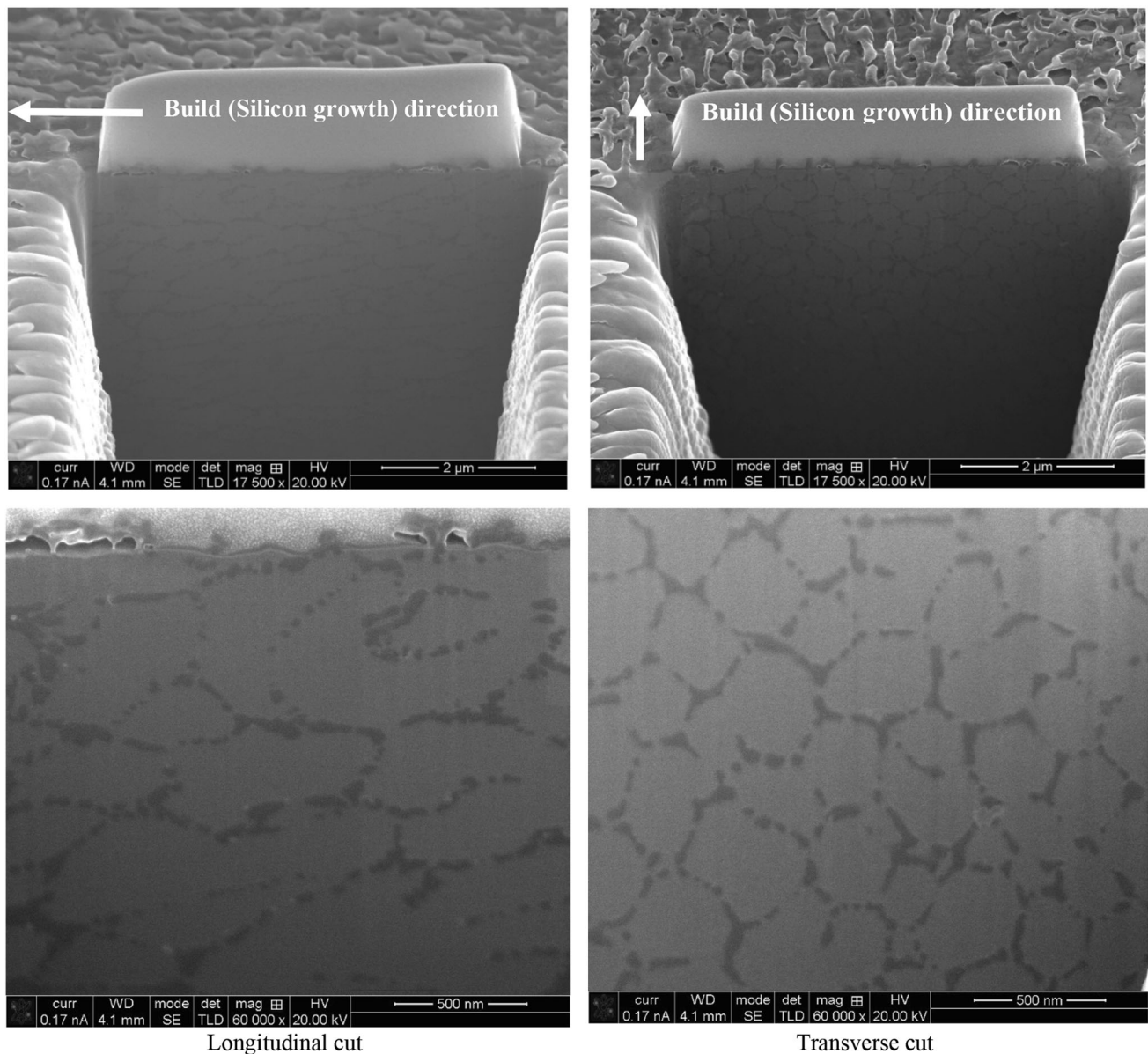
Fig. 15 FIB wedge cut in directions along and perpendicular to Si phase growth direction of the eutectic mixture of as-printed tensile coupons prepared in Y-direction

estimate the cooling rate, growth rate, temperature gradient, and undercooling during L-PBF 3D printing of Al12Si alloy. It has been established that the Al–Si eutectic has a divorced architecture attributed to the difficulty associated with Si growth resulted from rapid solidification and short diffusion path and the nature of Si interface (smooth faceted interface) where adding atoms at Si interface are not as straightforward as for Al with a diffuse (rough) interface. The very rapid cooling of melt pool (Cooling rate— $\dot{T} \sim 1.1 \times 10^6$ °C/s, growth rate—$R \sim 140$ mm/s, undercooling—$\Delta T \sim 70$ °C and temperature gradient—$G \sim 7700$ °C/mm (7.7 °C/μm)) during L-PBF printing results in increasing the degree of super saturation of Si in primary Al phase which is expected to improve the alloy response to post heat treatment. The eutectic Si has a spongy character with fine particles agglomerated to form the overall morphology of eutectic Si. It has clearly shown that the eutectic Si does not have the fibrous morphology reported during chill casting (rapid cooling) or chemical modification for conventional casting routes.

References

1. J. Smith et al., Linking Process, Structure, Property, and Performance for Metal-Based Additive Manufacturing: Computational Approaches with Experimental Support, *Comput. Mech.*, 2016, **57**(4), p 583–610
2. B. Zhang, Y. Li, and Q. Bai, Defect Formation Mechanisms in Selective Laser Melting: A Review, *Chin. J. Mech. Eng.*, 2017, **30**(3), p 515–527
3. H. Patrick and E. Mohsen, Effect of Build Orientation on the Microstructure and Mechanical Properties of Selective Laser-Melted Ti-6Al-4V Alloy, *J. Manuf. Mater. Process.*, 2018, **2**(4), p 69
4. A.D. Baghi, S. Nafisi, R. Hashemi, H. Ebendorff-Heidepriem, and R. Ghomashchi, Experimental Realisation of Build Orientation Effects on the Mechanical Properties of Truly as-Built Ti-6Al-4V SLM Parts, *J. Manuf. Process.*, 2021, **64**, p 140–152
5. A.D. Baghi, S. Nafisi, R. Hashemi, H. Ebendorff-Heidepriem, and R. Ghomashchi, Effective Post Processing of SLM Fabricated Ti-6Al-4 V Alloy: Machining vs Thermal Treatment, *J. Manuf. Process.*, 2021, **68**, p 1031–1046
6. X.P. Li, C.W. Kang, H. Huang, L.C. Zhang, and T.B. Sercombe, Selective Laser Melting of an $Al_{86}Ni_6Y_{4.5}Co_2La_{1.5}$ Metallic Glass: Processing, Microstructure Evolution and Mechanical Properties, *Mater. Sci. Eng. A*, 2014, **606**, p 370–379
7. X.P. Li, C.W. Kang, H. Huang, and T.B. Sercombe, The Role of a Low-Energy–Density re-Scan in Fabricating Crack-Free $Al_{85}Ni_5Y_6Co_2Fe_2$ Bulk Metallic Glass Composites via Selective Laser Melting, *Mater. Des.*, 2014, **63**, p 407–411
8. T. Vilaro, V. Kottman-Rexerodt, M. Thomas, C. Colin, P. Bertrand, L. Thivillon et al., Direct Fabrication of a Ti-47Al-2Cr-2Nb Alloy by Selective Laser Melting and Direct Metal Deposition Processes, *Adv. Mater. Res.*, 2010, **89–91**, p 586–591
9. Y. Li and D. Gu, Parametric Analysis of Thermal Behavior During Selective Laser Melting Additive Manufacturing of Aluminum Alloy Powder, *Mater. Des.*, 2014, **63**, p 856–867
10. P.A. Kobryn and S.L. Semiatin, The Laser Additive Manufacture of Ti-6Al-4V, *JOM*, 2001, **53**(9), p 40–42
11. P.A. Hooper, Melt Pool Temperature and Cooling Rates in Laser Powder Bed Fusion, *Addit. Manuf.*, 2018, **22**, p 548–559
12. L. Cheng, J. Bai, and A.C. To, Functionally Graded Lattice Structure Topology Optimization for the Design of Additive Manufactured Components with Stress Constraints, *Comput. Methods Appl. Mech. Eng.*, 2019, **344**, p 334–359
13. W. Xu, M. Brandt, S. Sun, J. Elambasseril, Q. Liu, K. Latham, K. Xia, and M. Qian, Additive Manufacturing of Strong and Ductile Ti–6Al–4V by Selective Laser Melting via In Situ Martensite Decomposition, *Acta Mater.*, 2015, **85**, p 74–84
14. H. Attar, M. Calin, L.C. Zhang, S. Scudino, and J. Eckert, Manufacture by Selective Laser Melting and Mechanical Behavior of Commercially Pure Titanium, *Mater. Sci. Eng. A*, 2014, **593**, p 170–177
15. X.P. Li, X.J. Wang, M. Saunders, A. Suvorova, L.C. Zhang, Y.J. Liu, M.H. Fang, Z.H. Huang, and T.B. Sercombe, A Selective Laser Melting and Solution Heat Treatment Refined Al-12Si Alloy with a Controllable Ultrafine Eutectic Microstructure and 25% Tensile Ductility, *Acta Mater.*, 2015, **95**, p 74–82
16. S. Nafisi, D. Emadi, and R. Ghomashchi, Semi Solid Metal Processing: The Fraction Solid Dilemma, *Mater. Sci. Eng. A*, 2009, **507**, p 87–92
17. T. El-Benawy and H. Fredriksson, Solidification Mechanism of Unmodified and Strontium Modified Al-Si Alloys, *Mater. Trans. JIM*, 2000, **41**(4), p 507–515
18. R. Elliot, *Eutectic Solidification Process*, Butterworth, London, 1983
19. S. Nafisi and R. Ghomashchi, *Semi-Solid Processing of Aluminum Alloys*, Springer, Cham, 2016. https://doi.org/10.1007/978-3-319-40335-9
20. S. Nafisi, R. Ghomashchi, and H. Vali, Eutectic Nucleation in Hypoeutectic Al-Si Alloys, *Mater. Charact.*, 2008, **59**, p 1466–1473
21. S.-Z. Lu and A. Hellawell, The Mechanism of Silicon Modification in Aluminum-Silicon Alloys: Impurity Induced Twinning, *Met. Trans. A*, 1987, **18A**, p 1721–33
22. L.M. Hogan and M. Shamsuzzoha, Crystallography of the Flake-Fiber Transition in the Al-Si Eutectic, *Mater. Forum*, 1987, **10**, p 270–277
23. K. Nogita, S.D. McDonald, K. Tsujimoto, K. Yasuda, and A.K. Dahle, Aluminum Phosphide as a Eutectic Nucleus in Hypoeutectic Al-Si Alloys, *J. Electron. Microsc.*, 2004, **53**, p 361–369
24. S. Shankar, Y.W. Riddle, and M.M. Makhlouf, Nucleation Mechanism of the Eutectic Phases in Aluminum-Silicon Hypoeutectic Alloys, *Acta Mater.*, 2004, **52**, p 4447–4460
25. W. Kurz and D.J. Fisher, Dendrite Growth in Eutectic Alloys: The Coupled Zone, *Int. Met. Rev.*, 1979, **5&6**, p 177–204
26. S. Nafisi and R. Ghomashchi, Boron-Based Refiners: Advantages in Semi-solid-Metal Casting of Al-Si Alloys, *Mater. Sci. Eng. A*, 2007, **452–453**, p 437–444
27. M.R. Ghomashchi, High Pressure Die-Casting: Effect of Fluid Flow on the Microstructure of LM24 Die-Casting Alloy, *J. Mat. Process. Technol.*, 1995, **52**(2–4), p 193–206
28. M.R. Ghomashchi and A. Vikhrov, Squeeze Casting: An Overview, *J. Mater. Process. Technol.*, 2000, **101**, p 1–9
29. N.T. Aboulkhair, M. Simonelli, L. Parry, I. Ashcroft, C. Tuck, and R. Hague, 3D printing of Aluminium Alloys: Additive Manufacturing of Aluminium Alloys Using Selective Laser Melting, *Prog. Mater. Sci.*, 2019, **106**, p 100578
30. J. Zhang, Bo. Songa, Q. Wei, D. Bourell, and Y. Shi, A Review of Selective Laser Melting of Aluminum Alloys: Processing, Microstructure, Property and Developing Trends, *J. Mater. Sci. Technol.*, 2019, **35**, p 270–284
31. A.B. Anwar and Q.-C. Pham, Selective Laser Melting of AlSi10Mg: Effects of Scan Direction, Part Placement and Inert Gas Flow Velocity on Tensile Strength, *J. Mater. Process. Technol.*, 2017, **240**, p 388–396
32. L.P. Lam et al., Phase Analysis and Microstructure Characterisation of AlSi10Mg Parts Produced by Selective Laser Melting, *Virtual Phys. Prototyp.*, 2015, **10**(4), p 207–215
33. B. Chen et al., Strength and Strain Hardening of a Selective Laser Melted AlSi10Mg Alloy, *Scr. Mater.*, 2017, **141**, p 45–49
34. M. Fousová et al., Changes in the Microstructure and Mechanical Properties of Additively Manufactured AlSi10Mg Alloy After Exposure to Elevated Temperatures, *Mater. Character.*, 2018, **137**, p 119–126
35. E. Vandersluis, P. Emadi, B. Andilab, and C. Ravindran, The Role of Silicon Morphology in the Electrical Conductivity and Mechanical Properties of As-Cast B319 Aluminum Alloy, *Metall. Mater. Trans. A.*, 2020, **51**, p 1874–1886
36. ASTM International, *ASTM E8/E8M-16a, Standard Test Methods for Tension Testing of Metallic Materials*, ASTM International, West Conshohocken, 2016
37. R. Ghomashchi, Advanced Mechanics of Materials: Introduction to Composite materials. In: Lecture Notes, University of Adelaide (2011–2022)
38. Z. Wang, H. Wang, M. Yang, W. Sun, G. Yin, Q. Zhang, and Z. Ren, Thermal Reliability of Al-Si Eutectic Alloy for Thermal Energy Storage, *Mater. Res. Bull.*, 2017, **95**, p 300–306
39. S. Liu, J. Zhu, H. Zhu, J. Yin, C. Chen, and X. Zeng, Effect of the Track Length and Track Number on the Evolution of the Molten Pool Characteristics of SLMed Al Alloy: Numerical and Experimental Study, *Opt. Laser Technol.*, 2020, **123**, p 105924
40. E. Louvis, P. Fox, and C.J. Sutcliffe, Selective Laser Melting of Aluminium Components, *J. Mater. Process. Technol.*, 2011, **211**, p 275–284

41. R.C. Weast and S.M. Selby, *CRC Handbook of Chemistry and Physics*, CTC Press, Boca Raton, 1981

42. W.E. King, A.T. Anderson, R.M. Ferencz, N.E. Hodge, C. Kamath, S.A. Khairallah, and A.M. Rubenchik, Laser Powder Bed Fusion Additive Manufacturing of Metals; Physics, Computational, and Materials Challenges, *Appl. Phys. Rev.*, 2015, **2**, p 041304

43. J. Carvill, in Mechanical Engineer's Data Handbook, @ 20°C and 1 bar (1993)

44. Y. Sun, H. Muta, K. Kurosaki, and Y. Ohishi, Thermal and Electrical Conductivity of Liquid Al-Si Alloys, *Int. J. Thermophys.*, 2019, **40**, p 1–10

45. R. Brandt and G. Neuer, Electrical Resistivity and Thermal Conductivity of Pure Aluminum and Aluminum Alloys Up to and Above the Melting Temperature, *Int. J. Thermophys.*, 2007, **28**, p 1429

46. B.M. Angadi, C.R. Hiremath, A.C. Reddy, V.V. Katti, and S.A. Kori, Studies on the Thermal Properties of Hypereutectic Al-Si Alloys by Using Transient Method, *J. Mech. Eng.*, 2014, **2**(1), p 536–544

47. D. Dai, Gu. Dongdong, Q. Ge, Y. Li, X. Shi, Y. Sun, and S. Li, Mesoscopic Study of Thermal Behavior, Fluid Dynamics and Surface Morphology During Selective Laser Melting of Ti-Based Composites, *Comput. Mater. Sci.*, 2020, **177**, p 109598

48. P. Yuan and Gu. Dongdong, Molten Pool Behaviour and Its Physical Mechanism During Selective Laser Melting of TiC/AlSi10Mg Nanocomposites: Simulation and Experiments, *J. Phys. D Appl. Phys.*, 2015, **48**, p 035303

49. M.C. Flemings, *Solidification Processing*, McGraw-Hill, New York, 1974, p 109

50. W. Kurz and D.J. Fisher, *Fundamentals of Solidification*, 3rd ed. Trans Tech Publications, Wollerau, 1989, p 54

51. J. Qin, X. Li, J. Wang, and S. Pan, The Self-Diffusion Coefficients of Liquid Binary M-Si(M = Al, Fe, Mg and Au) Alloy Systems by First Principles Molecular Dynamics Simulation, *AIP Adv.*, 2019, **9**, p 035328

52. B. Toloui and A. Hellawell, Phase Separation and Undercooling in Al-Si Eutectic Alloy: The Influence of Freezing Rate and Temperature Gradient, *Acta Metall.*, 1976, **24**, p 565

53. R.T. Dehoff, Measurement of Number and Average Size in Volume, *Book: Quantitative Microscopy*. R.T. Dehoff, F.N. Rhines Ed., McGraw Hill, New York, 1986, p 131

54. R. Ghomashchi and S. Nafisi, Some Remarks on Cooling Curves as a Principle Tool for Solidification Characterization, *J. Cryst. Growth*, 2017, **458**, p 129–132

55. H. Kobatake, J. Brillo, J. Schmitz, and P.-Y. Pichon, Surface Tension of Binary Al–Si Liquid Alloys, *J. Mater. Sci.*, 2015, **50**, p 3351–3360

56. G.A. Chadwick, *Metallography of Phase Transformations*, Butterworths, London, 1972, p 80

57. W. Kurz and R. Trivedi, Rapid Solidification Processing and Microstructure Formation, *Mater. Sci. Eng. A*, 1994, **179**, p 46–51

58. H. Bracht and E.E. Haller, Silicon Self-Diffusion in Isotope Heterostructures, *Phys. Rev. Lett.*, 1998, **81**(2), p 393